

Polycyclic aromatic hydrocarbon (PAH) luminous galaxies in JWST CEERS data

Yu-Wei Lin¹, Cossas K.-W. Wu^{1,2}, Chih-Teng Ling^{1,2}, Tomotsugu Goto^{1,2}, Seong Jin Kim², Ece Kilerci³, Tetsuya Hashimoto⁴, Po-Ya Wang¹, Simon C.-C. Ho^{5,6,7,8}, Tiger Yu-Yang Hsiao⁹, Bjorn Jasper R. Raquel^{4,10}, and Yuri Uno⁴

¹Department of Physics, National Tsing Hua University, 101, Section 2, Kuang-Fu Road, Hsinchu, 30013, Taiwan (R.O.C.)

²Institute of Astronomy, National Tsing Hua University, 101, Section 2, Kuang-Fu Road, Hsinchu, 30013, Taiwan (R.O.C.)

³Sabancı University, Faculty of Engineering and Natural Sciences, 34956, Istanbul, Turkey

⁴Department of Physics, National Chung Hsing University, 145, Xingda Road, Taichung, 40227, Taiwan (R.O.C.)

⁵Research School of Astronomy and Astrophysics, The Australian National University, Canberra, ACT 2611, Australia

⁶Centre for Astrophysics and Supercomputing, Swinburne University of Technology, P.O. Box 218, Hawthorn, VIC 3122, Australia

⁷OzGrav: The Australian Research Council Centre of Excellence for Gravitational Wave Discovery, Hawthorn, VIC 3122, Australia

⁸ASTRO3D: The Australian Research Council Centre of Excellence for All-sky Astrophysics in 3D, ACT 2611, Australia

⁹Department of Physics and Astronomy, The Johns Hopkins University, 3400 N Charles St. Baltimore, MD 21218, USA

¹⁰Department of Earth and Space Sciences, Rizal Technological University, Boni Avenue, Mandaluyong, 1550 Metro Manila, Philippines

Accepted 2023 December 22. Received 2023 December 22; in original form 2023 May 08

ABSTRACT

It has been an unanswered question how many dusty galaxies have been undetected from the state-of-the-art observational surveys. *JWST* enables us to detect faint IR galaxies that have prominent polycyclic aromatic hydrocarbon (PAH) features in the mid-IR wavelengths. PAH is a valuable tracer of star formation and dust properties in the mid-infrared wavelength. The *JWST* Cosmic Evolution Early Release Science (CEERS) fields provide us with wavelength coverage from 7.7 to 21 μm using six photometric bands of the mid-infrared instrument (MIRI). We have identified galaxies dominated by mid-IR emission from PAHs, termed PAH galaxies. From our multi-band photometry catalogue, we selected ten PAH galaxies displaying high flux ratios of $\log(S_{15}/S_{10}) > 0.8$. The SED fitting analysis indicates that these galaxies are star-forming galaxies with total IR luminosities of $10^{10} \sim 10^{11.5} L_{\odot}$ at $z \sim 1$. The morphology of PAH galaxies does not show any clear signatures of major merging or interaction within the MIRI resolution. The majority of them are on the star-formation main sequence at $z \sim 1$. Our result demonstrates that *JWST* can detect PAH emissions from normal star-forming galaxies at $z \sim 1$, in addition to ultra-luminous infrared galaxies (ULIRGs) or luminous infrared galaxies (LIRGs).

Key words: galaxies: photometry, galaxies: star formation, infrared: galaxies

1 INTRODUCTION

Polycyclic aromatic hydrocarbons (PAHs) are chemical compounds based on the Benzene structure (C_6H_6 , ‘aromatic ring’) composed of hydrogen and carbon atoms (Candian et al. 2018). These molecules are known to absorb UV/optical light and re-emit infrared (IR) photons via vibration modes, which produce broad features at 3.3, 6.2, 7.7, 8.6, 11.3, 12.7 and 17 μm in the IR spectrum of local galaxies (Tielens 2008; Li 2020; Kwok 2022). Due to this property, PAHs serve as good tracers for star formation rate (SFR) (Rigopoulou et al. 1999; Peeters et al. 2003, 2006). Consequently, it is expected that galaxies with high SFRs will exhibit luminous PAH features. PAH luminous galaxies are expected to have SFRs (Desai et al. 2007; Elbaz et al. 2011; Takagi et al. 2011; Kim et al. 2019; Armus et al. 2020), as the overall strength of the PAH emission features is a good tracer of the star-formation activity in galaxies. However, at a redshift of $z = 1$, the PAH features shift to 6.6, 12.4, 15.4, 17.2, 22.6, 25.4 and 34 μm , respectively, resulting in a photometric excess in

the mid-IR band, which has a high flux density ratio between observation filters such as $S_{15}/S_{10} > 10^{0.8}$. The James Webb Space Telescope (*JWST*) is a state-of-the-art infrared (IR) telescope with a 6.5-meter mirror (Gardner et al. 2006; Kalirai 2018; McElwain et al. 2023; Wright et al. 2023; Gardner et al. 2023), possessing high sensitivity and spatial resolution. As such, it presents a unique opportunity to select fainter and more distant galaxies displaying mid-IR excess compared to the *AKARI* and *Spitzer* telescopes. In particular, recent studies (Ling et al. 2022; Wu et al. 2023; Hsiao et al. 2023a,b) have demonstrated the potential for *JWST* observations to provide improved insight into the nature of galaxies.

The majority of PAH galaxies suffer from statistical bias towards more luminous populations, e.g., luminous IR galaxies (LIRGs, $L_{\text{IR}} = 10^{11} - 10^{12} L_{\odot}$), and ultra-luminous IR galaxies (ULIRGs, $L_{\text{IR}} = 10^{12} - 10^{13} L_{\odot}$) (Elbaz et al. 2005, 2007), up to peak of the star-formation rate density (SFRD) (Weedman & Houck 2008; Shipley et al. 2016). The majority of these galaxies are star-forming galaxies on the main sequence (MS) with a smaller fraction of starbursts

(SB) above the MS at different redshifts (Elbaz et al. 2007, 2011; Whitaker et al. 2012; Pearson, W. J. et al. 2018; Popesso et al. 2023). However, research on less luminous sources with $L_{\text{IR}} < 10^{11} L_{\odot}$, such as normal/faint galaxies at similar/higher redshifts, is limited. In this work, we aim to identify and investigate the properties of such galaxies, including their star formation rates, stellar masses and morphology.

JWST is a game changer which has opened up a new era and enables us to observe faint IR galaxies that were beyond the detection limits of previous generation space telescopes such as *AKARI* and *Spitzer*. With *JWST*, we are now able to peer/select normal/faint IR galaxies that have prominent PAHs even at $z \sim 1$. In this work, we show one of the first such analyses using the *JWST* early release observations.

This paper is organised as follows: In Section 2 we present the properties of *JWST* CEERS field data and spectral energy distribution (SED) model. In Section 3, we show the SED fitting results by CIGALE (Boquien et al. 2019), and we compare the physical properties of PAH luminous galaxies to the literature in Section 4. Finally, our conclusion is given in Section 5. A flat cosmology with $H_0 = 70 \text{ km s}^{-1} \text{ Mpc}^{-1}$, $\Omega_m = 0.3$ and $\Omega_{\Lambda} = 0.7$ is used. All magnitudes are given in the AB system.

2 DATA AND METHODS

2.1 Data

We utilise the *JWST* MIRI 6 bands observations at 7.7, 10.0, 12.8, 15.0, 18.0, and 21.0 μm (F770W, F1000W, F1280W, F1500W, F1800W, and F2100W) in the Cosmic Evolution Early Release Science (CEERS) fields (Finkelstein et al. 2017). We used the two sub-fields of CEERS (i.e., jw01345-o001 and jw01345-o002) which cover 2 arcmin² each and 4 arcmin² in total. The detection limits in these 6 bands are 0.20, 0.40, 0.79, 1.3, 4.0, and 10 μJy from F770W to F2100W, respectively. The details for source extraction are described in (Wu et al. 2023). We cross-match *JWST* sources to the Cosmic Assembly Near-infrared Deep Extragalactic Legacy Survey (CANDELS) Extended Groth Strip (EGS) field (Stefanon et al. 2017). The CANDELS-EGS gathered multi-wavelength photometric data ranging from ultraviolet to infrared wavelengths, observed using six different instruments. The UV data (u^* , g' , r' , i , z') were obtained through Canada–France–Hawaii Telescope (CFHT) MegaCam observations, while the NOAO Extremely Wide-Field Infrared Imager (NEWFIRM) Medium-Band Survey (NMBS) provided additional photometry. The NIR band (J , H , and K_s) data were acquired through CFHT Wide-field InfraRed Camera (WIRCam) observations, while the Hubble Space Telescope (HST) Advanced Camera for Surveys (ACS) and HST Wide Field Camera 3 (WFC3) provided 5 bands of photometry from optical to NIR. Finally, *Spitzer* IRAC observations provided 4 bands of photometry from 3 to 8 μm , detail of the catalogue is described in Stefanon et al. (2017). In Table 1, we present the main properties of the 21 bands data set which we used to perform the SED fitting.

2.2 Sample selection

In Fig. 1, we show the colour-colour plot between S_{15}/S_{10} and $S_{10}/S_{7.7}$. We select sources based on detection in 3 MIRI bands F770W, F1000W, and F1500W. There are 155 sources in these three bands. We utilise the method from Takagi et al. (2010) to select 15 μm flux density excess sources that are likely PAH galaxies. The

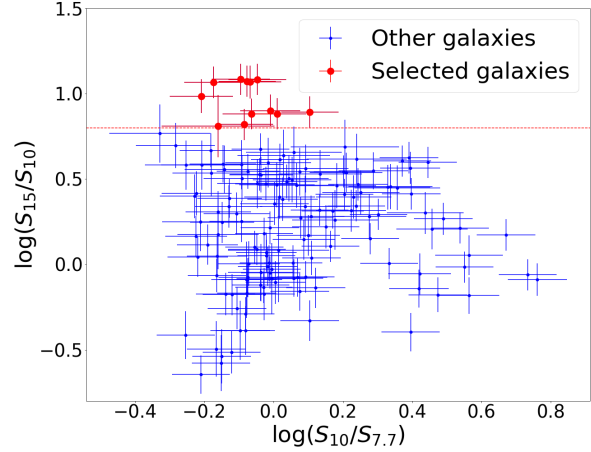


Figure 1. A colour-colour plot of three-bands-detected (7.7, 10, and 15 μm) source with 15-to-10 μm and 10-to-7.7 μm flux ratios. The red dashed line indicates the criteria cut to select the PAH sources from Takagi et al. (2010). The red points indicate the PAH-selected galaxies.

selection criterion for the sample is the ratio of flux density between 15-to-10 μm greater than 0.8 (dex), or $\log(S_{15}/S_{10}) > 0.8$ from (Takagi et al. 2010), indicated by the red dashed line in Fig. 1. In total, we identify 12 galaxies that meet the selection criteria.

2.3 CIGALE SED fitting

We utilise the Code Investigating GALaxy Emission (CIGALE, Boquien et al. 2019) to fit the spectral energy distribution (SED) of galaxies. In the energy balance principle, the stellar light emitted in UV/optical is absorbed by dust and re-emitted in the mid- to far-IR. CIGALE fits the multi-wavelength band photometric data based on the energy balance principle using various modules (e.g., Boquien et al. 2019; Wang et al. 2020; Santos et al. 2021). We utilise CIGALE version 2020.0 to fit the SEDs with models in Table 2 such as star formation history (SFH), attenuation law, dust emission, and single stellar population (SSP). Important quantities obtained by CIGALE such as the photometric redshift, total infrared luminosity, and star formation rate (SFR) are presented in Table 3. We utilise the delayed SFH optional exponential burst from Boquien et al. (2019). We adopt the stellar templates from Bruzual & Charlot (2003) with the initial mass function Salpeter (1955). The dust attenuation model follows Charlot & Fall (2000) with additional flexibility. The attenuation law model is contributed by the birth cloud and the interstellar medium (ISM) with two power laws (Lo Faro et al. 2017) and (Buat et al. 2018), and we set slope flexibility. In addition, we parameterised the ISM V-band attenuation (A_V^{ISM}) and the $\mu = 0.44$ based on (Malek, K. et al. 2018). The dust absorbed from UV/optical and re-emitted into IR is modelled from dust templates of (Draine et al. 2014). Finally, we incorporated the AGN emission model module proposed by Fritz et al. (2006), which employs a radiative transfer model incorporating three key components: (1) the primary source of radiation situated within the torus, (2) the scattered emission by dust, and (3) the thermal dust emission, as described by Boquien et al. (2019). Compared to (Santos et al. 2021), we tried a slightly larger number of parameters (e.g., 0.1 for optical depth; 0.0 for beta in gas density; 0.0 for gamma in gas density; 60 for opening angle; 0.001 for the angle

Table 1. Summary of 21 bands for CIGALE SED fitting.

Band	Instrument	Wavelength (μm)	Depth 5σ (mag)	Reference
u^*	CFHT/MegaCam	0.383	27.1	Gwyn (2012)
g'	CFHT/MegaCam	0.489	27.3	Gwyn (2012)
r'	CFHT/MegaCam	0.625	27.2	Gwyn (2012)
i'	CFHT/MegaCam	0.769	27.0	Gwyn (2012)
z'	CFHT/MegaCam	0.888	26.1	Gwyn (2012)
F606W	HST/ACS	0.596	28.8	Koekemoer et al. (2011)
F814W	HST/ACS	0.809	28.2	Koekemoer et al. (2011)
F125W	HST/WFC3	1.250	27.6	Koekemoer et al. (2011)
F140W	HST/WFC3	1.397	26.8	Brammer et al. (2012); Skelton et al. (2014)
F160W	HST/WFC3	1.542	27.6	Koekemoer et al. (2011)
J	WIRCam	1.254	24.4	Bielby, R. et al. (2012)
H	WIRCam	1.636	24.5	Bielby, R. et al. (2012)
K_s	WIRCam	2.159	24.3	Bielby, R. et al. (2012)
IRAC1	<i>Spitzer</i>	3.6	21.8	Ashby et al. (2015)
IRAC2	<i>Spitzer</i>	4.5	22.4	Ashby et al. (2015)
F770W	JWST/MIRI	7.7	25.4	Wu et al. (2023)
F1000W	JWST/MIRI	10.0	24.6	Wu et al. (2023)
F1280W	JWST/MIRI	12.8	24.0	Wu et al. (2023)
F1500W	JWST/MIRI	15.0	23.5	Wu et al. (2023)
F1800W	JWST/MIRI	18.0	22.7	Wu et al. (2023)
F2100W	JWST/MIRI	21.0	22.1	Wu et al. (2023)

between equatorial axis and line of sight). The redshifting module contains the K-correction to estimate the photometric redshift (Boquien et al. 2019). The photometric redshift is a free parameter in the SED fitting with an interval of 0.01 for $z = 0 - 2$, and 0.1 for $z = 2 - 20$.

3 RESULTS

We identify a subsample of 10 PAH luminous galaxies through SED fitting using CIGALE. These galaxies are selected based on a reduced chi-square (χ^2) less than 6 to ensure reliable fitting results. Two galaxies which do not meet the criterion are excluded, as shown in Fig. A10, A11. The estimated physical properties of the galaxies are listed in Table 3. The AGN contribution obtained from CIGALE is zero for these ten sources, and ID 66 and 136 have 0.025. Since AGN contribution is very small (less than 2.5%), we regard dust luminosity from CIGALE as total infrared luminosity. In Fig. 2, we show cutout images ($2'' \times 2''$) at six MIRI bands of our ten PAH-selected galaxies, and the pixel scale is $0.11''$. These are classified as extended sources with CLASS_STAR < 0.5 in the EGS catalogue (Stefanon et al. 2017). We note that our MIRI imaging does not provide the required resolution to conclude if these galaxies are interacting systems. As reported by Huang et al. (2023, Fig. 1) NIRCam imaging can provide the necessary resolution at $z \sim 1-2$ to analyse the detailed morphologies of these galaxies. In Fig. 3, we present an example (ID59 in the Table 3) of the SED fitting result from CIGALE. The model spectrum (black solid line) is mainly composed of two primary components: stellar emission (blue dashed line) and dust emission (red solid line). We also analyse the photometric redshift and the reduced chi-square (χ^2). In Fig. 4, we show the redshift against the flux density ratio between S_{15} and S_{10} for all sources in the JWST CEERS field. Using galaxy SED models from Polletta et al. (2007), we show how S_{15}/S_{10} of typical galaxy types evolve as a function of redshift, presenting a comparison with the observed data points. The SED model templates

used here are a spiral galaxy (Sd) as a normal star-forming galaxy (SFG), M82 as a starburst, NGC6090 (similar to M82 but showing much stronger PAHs), and Seyfert type2 as a composite. It shows that our sample galaxies are located much higher than what we can expect from the galaxy types we know. The red points, representing the PAH luminous galaxies, are located around $z \sim 1$. As the rest-frame PAH $7.7 \mu\text{m}$ features shift to $15.4 \mu\text{m}$ at $z = 1$, this is expected by selecting $15 \mu\text{m}$ excess sources.

4 DISCUSSION

4.1 Colour Selection

Kirkpatrick et al. (2017) generated the synthetic galaxies from a MIR-based template library (Kirkpatrick et al. 2015). The template library comprises 11 templates derived from spectroscopic sources observed with *Spitzer* and *Herschel*. Kirkpatrick et al. (2017) utilised 5500 synthetic galaxies to establish JWST MIRI colour combination criteria for three distinct populations AGNs, Composite, and SFGs for galaxies within the redshift range of 1 to 2. In Fig. 5, $S_{15}/S_{7.7-18}/S_{10}$ colour-colour plot for JWST sources, and two black contours indicate the selection criteria at $z = 0.75-1.25$ from Kirkpatrick et al. (2017, Eq.1). AGNs are located inside the small circle, composites are located between the two circles, and SFGs are located outside the big circle. Red dots represent our ten PAH luminous galaxies, with 9 of 10 sources located in the SFG region, and one source located in the composite region. Note, however, that these boundaries are not clear cuts, but rather a transitional area, where galaxies can mix in and out. None of the PAH galaxies we have selected is in their AGN circle, indicating that our criteria have successfully selected star-forming galaxies without significant contamination from AGN.

Table 2. List of modules and parameter settings for our CIGALE SED fitting.

Parameters	Value
<i>Delayed SFH with optional exponential burst (Boquien et al. 2019)</i>	
e-folding time of the main stellar population [10^6 yr]	2000.0, 5000.0, 10000.0
Age of the galaxy's main stellar population [10^6 yr]	1000.0, 2000.0, 5000.0, 10000.0
e-folding time of the late starburst population [10^6 yr]	200.0, 500.0, 2000.0, 20000.0
Age of the late burst [10^6 yr]	10.0, 20.0
Mass fraction of the late burst population	0.00, 0.01, 0.05, 0.1
multiplicative factor controlling the amplitude of SFR if normalisation is True	1.0
<i>SSP (Bruzual & Charlot 2003)</i>	
Initial mass function	Salpeter (1955)
Metallicity	0.02
Age of separation between the young and old star populations	10.0
<i>Dust attenuation (Charlot & Fall 2000)</i>	
Logarithm of the V-band attenuation in the ISM	0.1, 0.17, 0.28, 0.46, 0.77, 1.29, 2.15, 3.59, 5.99, 10.0
Ratio of V-band attenuation from old and young stars	0.44
Power-law slope of the attenuation in the ISM	-10.0, -5.0, -1, -0.9, -0.7, -0.5, -0.1
Power-law slope of the attenuation in the birth cloud	-10.0, -5.0, -3.0, -1.3, -1.0, -0.7
<i>Dust emission (Draine et al. 2014)</i>	
Mass fraction of PAH	0.47, 1.12, 1.77, 2.5, 3.19, 3.9, 4.58, 5.26, 5.95, 6.63, 7.32
Minimum radiation field (U_{\min})	0.1, 1.0, 10.0
Power-law slope α ($\frac{dU}{dM} \propto U^\alpha$)	1.0, 3.0
Fraction illuminated from U_{\min} to U_{\max}	0.01, 0.05, 0.1
<i>AGN emission (Fritz et al. 2006)</i>	
Ratio of the maximum and minimum torus radii	60.0
Optical depth at $9.7 \mu\text{m}$	0.1, 0.3, 6.0
Value of β in gas density gradient along the radial and polar distance coordinates (Eq. 3 in Fritz et al. 2006)	0.0, -0.5
Value of γ in gas density gradient along the radial and polar distance coordinates (Eq. 3 in Fritz et al. 2006)	0.0, 4
Opening angle of the torus	60.0, 100
Angle between equatorial axis and line of sight	0.001, 60.1, 89.99
AGN contribution fraction (frac_{AGN})	0.025 for 0.0 - 0.7
<i>Redshifting (Boquien et al. 2019)</i>	
Redshift	0.01 for $z = 0 - 2$, and 0.1 for $z = 2 - 20$

Table 3. The 10 PAH luminous galaxies SED fitting results

ID	RA	DEC	reduced chi-square(χ^2)	photometric redshift	$L_{\text{IR}} (L_{\odot})$	SFR ($M_{\odot}\text{yr}^{-1}$)	M (M_{\odot})
59	215.16776	53.051688	5.17	0.94	$5.11 \pm 3.05 \times 10^{10}$	12.67 ± 5.63	$2.86 \pm 0.56 \times 10^{10}$
64	215.158128	53.046943	1.37	1.0	$20.72 \pm 18.4 \times 10^{10}$	57.95 ± 53.22	$0.71 \pm 0.28 \times 10^{10}$
66	215.159489	53.048452	3.94	1.1	$38.92 \pm 2.0 \times 10^{10}$	49.12 ± 3.27	$12.31 \pm 0.74 \times 10^{10}$
72	215.160424	53.051557	2.75	1.1	$2.99 \pm 0.84 \times 10^{10}$	5.31 ± 1.31	$2.53 \pm 0.25 \times 10^{10}$
113	215.16312	53.064216	4.29	1.2	$11.39 \pm 5.32 \times 10^{10}$	16.45 ± 14.37	$3.91 \pm 0.5 \times 10^{10}$
136	215.145024	53.058089	3.26	1.22	$9.54 \pm 3.53 \times 10^{10}$	15.85 ± 6.07	$6.31 \pm 0.79 \times 10^{10}$
178	215.094758	52.983213	5.05	1.23	$43.5 \pm 12.45 \times 10^{10}$	62.92 ± 21.31	$6.7 \pm 1.04 \times 10^{10}$
187	215.075643	52.973745	1.76	1.21	$15.88 \pm 2.71 \times 10^{10}$	21.09 ± 4.83	$6.93 \pm 0.8 \times 10^{10}$
218	215.084489	52.990326	2.33	1.09	$6.3 \pm 3.69 \times 10^{10}$	10.14 ± 6.54	$1.62 \pm 0.5 \times 10^{10}$
225	215.068587	52.98334	4.75	0.78	$27.04 \pm 5.31 \times 10^{10}$	75.92 ± 15.49	$0.79 \pm 0.16 \times 10^{10}$

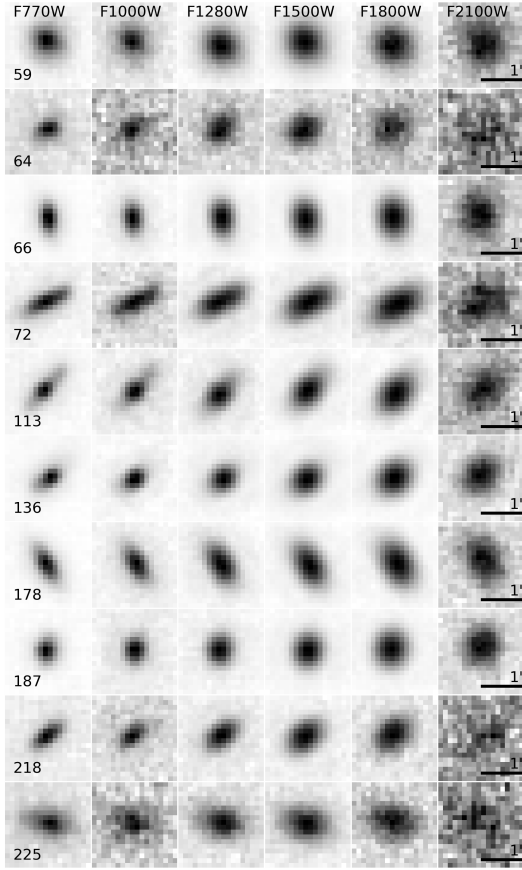


Figure 2. The *JWST* MIRI cutout images ($2'' \times 2''$) of our sample galaxies selected by the prominent PAH feature in the mid-IR. ID numbers (from Table 3) are given on the leftmost panel. The pixel scale is $0.11''$, and a small horizontal bar on the rightmost panel indicates the $1''$ size on the sky.

4.2 Obscured AGN or Compact obscured nuclei

Falstad et al. (2021) discussed the compact obscured nuclei (CON) with identifications of HCN molecule emission lines in the spectrum. García-Bernete et al. (2022b) discussed CONs with the PAH 6.2, 11.3 and $12.7 \mu\text{m}$ equivalent width (EW) ratio and $9.7 \mu\text{m}$ silicate absorption line, and performed the CONs criteria for the *JWST* MIR photometry observation at redshift from 0 to 1.5. In Fig. 6, we show the criteria from (García-Bernete et al. 2022b) given the CON-dominated regions on the colour-colour plot. We found none of our PAH galaxies are located in the CON region. In Sec.4.1, we compared the distribution of our sample with the colour criteria from Kirkpatrick et al. (2017) which classify their sample into AGN, composite, and SFG. Where should deep obscured AGN locate on the colour-colour plot? In Fig. 5, we calculate the dust extinction from (Gordon et al. 2023), and we show the extinction arrow $A_V = 10$ at $z \sim 1$. Due to the $9.7 \mu\text{m}$ silicate absorption, S_{18}/S_{10} colour at $z \sim 1$ becomes bluer by adding more extinction. If our sources experience

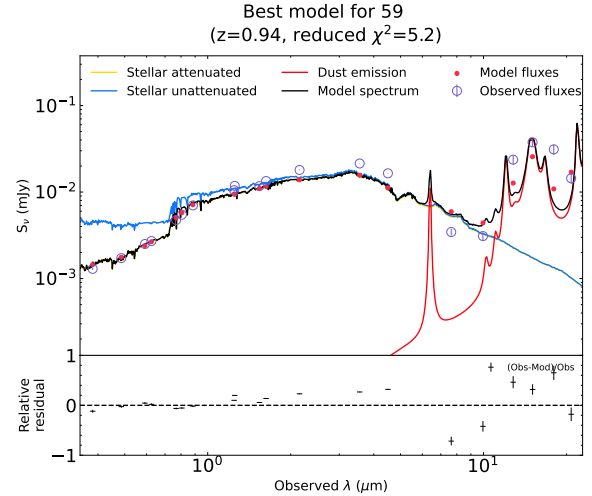


Figure 3. The SED fitting for ID 59 in the Table 3. The blue curve is the stellar emission and the red curve is the dust emission. The purple points are the observed photometry. The estimation of the photometric redshift was carried out simultaneously.

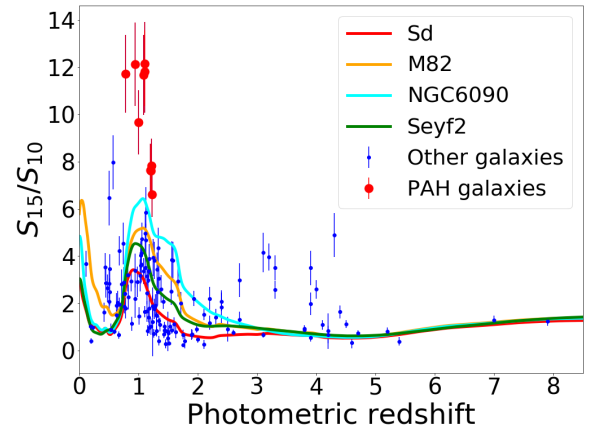


Figure 4. The distribution of the flux density ratio S_{15}/S_{10} for the CEERS MIR galaxies as a function of photometric redshift. Our sample galaxies (selected by " $15 \mu\text{m}$ excess", $\log(S_{15}/S_{10}) > 0.8$) are shown by the red dots. Curves represent the estimated evolution of S_{15}/S_{10} colour based on the SED model templates (Polletta et al. 2007). Spiral galaxy (Sd), a starburst having moderate PAHs (M82), a starburst showing stronger PAHs (NGC6090), and Seyfert 2 galaxy are shown. See the legend in the upper right box.

heavy dust attenuation, after the correction, the sources will shift in the top left direction, the opposite of the arrow direction. Therefore, in this colour, the selected PAH galaxies are not consistent with the AGN and the composite even after possible extinction correction, except for one galaxy that is already in the composite region.

4.3 Emission lines contribution to the F1000W and F1500W filters

We utilised the $15 \mu\text{m}$ excess to select the PAH luminous galaxies. However, in García-Bernete et al. (2022a,c); Rich et al. (2023) dis-

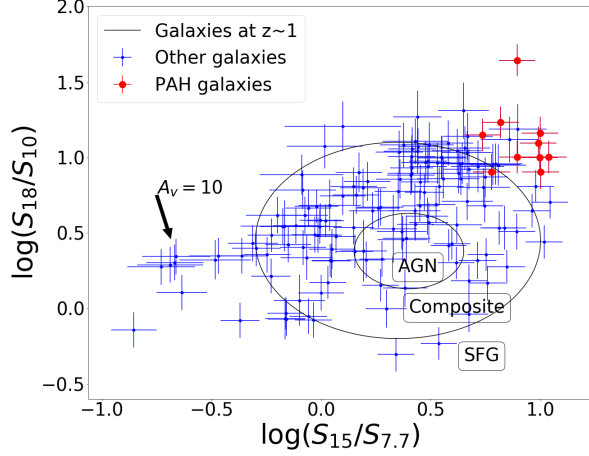


Figure 5. The AGN-Composite-SFG colour selection on $S_{18}/S_{10}-S_{15}/S_{7.7}$. The inner circle is the AGN criteria, and the outer circle is the SFG criteria from (Kirkpatrick et al. 2017). The region between the two circles is composites. The red points are the PAH luminous galaxies. The black arrow is the extinction $A_v = 10$.

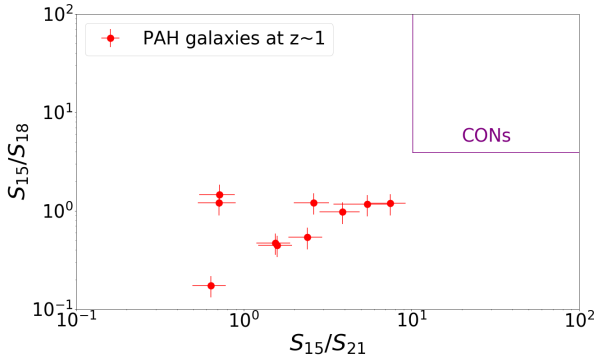


Figure 6. The CON dominated colour selection at $z \sim 1$ on $S_{15}/S_{21} - S_{15}/S_{18}$, and the selection is from (García-Bernete et al. 2022b). The purple square is the CON-dominated region.

cussed that the emission line gives the contribution to the photometry observation. Chasten et al. (2023a,b) discuss the CO, HI, and $H\alpha$ emission lines contribution. Rich et al. (2023) said that the AGN-dominated star-forming region shows extremely low 3.3 and 6.2 μm PAH equivalent width, and there are strong Pfund α emission lines at 7.46 μm . The excess in the photometry has the probability of contributing to the emission line. The *JWST* F1000W, F1500W filters have bandwidths of $\Delta\lambda$ 1.8, 2.92 μm , respectively. The half-power wavelengths, where the transmission falls to 50% of its peak value, range from 9.023 to 10.891 μm and 13.527 to 16.664 μm (Rieke et al. 2015). It is a concern that hydrogen emission lines might contribute to the flux in these filters, while our main focus is to estimate the effect of the PAH emissions. For galaxies at $z \sim 1$, five hydrogen emission lines fall into F1000W or F1500W filter broadband. In the F1500W filter at $z \sim 1$, two emission lines are observed, Pfund α at 7.46 μm , and Humphreys β at 7.49 μm . In the F1000W filter, three emission lines could contribute, Pfund β at 4.65 μm , and Humphreys (10-6)

and (11-6) at 5.13 and 4.67 μm . We estimate the contributions by utilising the SFR calculated by CIGALE as listed in Table 3. Following the Kennicutt (1998) Eq.2, we determined the $L_{H\alpha}$. We estimate contributions from the Pfund α and Humphreys β , assuming the CASE B recombination at $T = 10000\text{K}$, $N_e = 10000\text{cm}^{-3}$ (Hummer & Storey 1987). Our calculations revealed that the emission lines in the F1000W filter have contributions ranging from 0.01-2.4% for Pfund β and 0.006-1.15%, 0.005-0.88% for Humphreys (10-6), (11-6), respectively. In the F1500W filter, the contributions are 0.006-0.7% for Pfund α , and 0.001-0.2% for Humphreys β . Overall, the hydrogen recombination emission lines contribute less than 5% to the *JWST* F1000W, F1500W filters.

4.4 Star Formation Main Sequence

The main sequence (MS) is a correlation between SFR and stellar mass (M) of star-forming galaxies. MS evolution as a function of redshift is shown and discussed recently (Elbaz et al. 2007; Whitaker et al. 2012; Pearson, W. J. et al. 2018; Popesso et al. 2023). We calculated the SFR and M from CIGALE, listed in Table 3, and compared the results at the similar redshift bin with literature. In Fig. 7, Pearson, W. J. et al. (2018) gives MS in $z = 0.8 - 1.1$, $z = 1.1 - 1.4$, and Elbaz et al. (2007) gives $z = 0.8 - 1.2$. Whitaker et al. (2012) gives $z = 1 - 1.5$, and the outlier regions with other type galaxies. We overplot four galaxies between $0.8 < z < 1.5$ from the *AKARI* catalogue in (Kovács et al. 2019). Our samples plotted in red are mostly located in the main sequence, except for two galaxies in the upper left region as starbursts or composite. One of the two objects is the composite in Fig. 5. However, both have the AGN fraction=0 in CIGALE SED fitting. Note that CIGALE SED fitting utilises 21 available filters, in contrast to the colour-colour diagram which relies on only 4 filters. Therefore, we regard the CIGALE SED fitting as more informative. It is promising that even though Fig. 5 only utilises 4 colours, we have obtained consistent results from the remaining sources. Compared to previous data from the *AKARI*, and *Spitzer* telescope, *JWST* observed galaxies with less massive and smaller total IR luminosity.

4.5 PAH luminosity

At a redshift of $z \sim 1$, the PAH 7.7 μm feature in galaxies shifts to 15.4 μm , leading to a 15 μm -excess, which we used to identify PAH luminous galaxies (Takagi et al. 2010). To quantify the strength of PAH features in these galaxies, we employed a relation between PAH peak luminosity and total infrared luminosity for starburst, as established by (Houck et al. 2007; Weedman & Houck 2008). The equation is given as,

$$\log(\nu L_\nu(7.7\mu\text{m})) = \log(L_{IR}) - 0.78(\pm 0.2), \quad (1)$$

$\nu L_\nu(7.7\mu\text{m})$ is the PAH 7.7 μm peak luminosity which indicates the strength of PAH features in the galaxies, and L_{IR} is total IR luminosity. In our work, we computed L_{IR} from CIGALE SED fitting results shown in Table 3. We follow Houck et al. (2007); Kennicutt (1998) to estimate the PAH 7.7 μm peak luminosity at rest frame from CIGALE SED fitting results, the equation given as,

$$\nu L_\nu(7.7\mu\text{m}) = \frac{c}{\lambda_0} (1+z) \times \frac{4\pi d_L^2}{1+z} f_{\nu_0} = S_\nu(15\mu\text{m}) \times 9 \times 10^7 \times D_L^2 \div 7.7 \quad (2)$$

λ_0 is the rest-frame wavelength, here is 7.7 μm . f_{ν_0} is the observed flux density, here is 15 μm flux density. c is light speed. z is a photometric redshift. S_ν is the flux density of the PAH 15 μm peak value

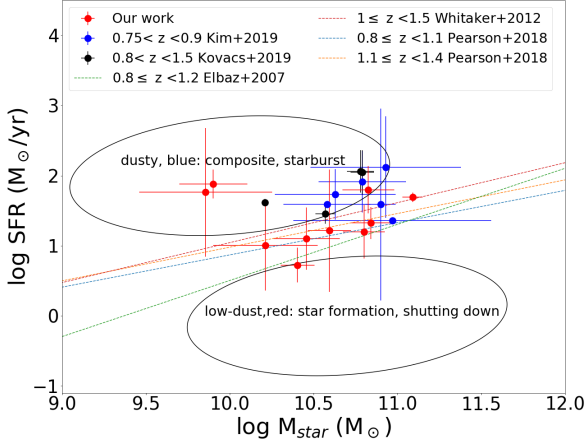


Figure 7. SFR - M_{\odot} correlation at $z \sim 1$. Both SFR and stellar mass are calculated from CIGALE. The dashed lines are the results with different redshift bins. The blue, and yellow lines are $z = 0.8 - 1.1$, $z = 1.1 - 1.4$ from (Pearson, W. J. et al. 2018). The green line is $z = 0.8 - 1.2$ from (Elbaz et al. 2007), and the red line is $z = 1 - 1.5$ from (Whitaker et al. 2012). Blue dots are from (Kim et al. 2019), and the black dots are from (Kovács et al. 2019). All of the points are located nearby the main sequence.

in the black line, shown in Fig. 3, and D_L is the luminosity distance calculated from photometric redshift within the cosmological model. Takagi et al. (2010) provided PAH-selected galaxies, which are LIRGs/ULIRGs, the orange points shown in Fig. 8, out of all the galaxies at $z > 1$ in the AKARI catalogue. In Fig. 8, we have the galaxies which have the one order fainter L_{IR} than those in the AKARI sample from (Takagi et al. 2010). We performed a least square fit in our work with the same coefficient, and the result is given as,

$$\log(\nu L_{\nu}(7.7\mu m)) = \log(L_{IR}) - 0.66(\pm 0.15). \quad (3)$$

Compared with (Houck et al. 2007; Weedman & Houck 2008) and (Takagi et al. 2010) observed galaxies by AKARI at $z \sim 1$, our result (red solid line) is located within 1-sigma (orange dashed line). Therefore, statistically, the correlations are consistent between our work and literature on the L_{PAH} to L_{IR} plane. In Fig. 8, we also compare with the local IR galaxies which are shown in black points and L_{PAH} to L_{IR} relation (Goto et al. 2011). Compared with all galaxies in our work, there are no significant differences between the two relations, which indicates the L_{PAH} to L_{IR} relation does not change significantly in these redshift and luminosity ranges.

Since PAH is a good tracer of the star-forming region in the Universe, there is a relation between PAH luminosity and SFR, which in turn relates SFR and L_{PAH} for SFGs. Numerous studies support this relationship, as evidenced by galaxy samples and observations at high redshift (Pope et al. 2008; Riechers et al. 2014; Shipley et al. 2016; Spilker et al. 2023). Pope et al. (2008) presented PAH luminosity as a proxy for the SFR in the submillimeter galaxies (SMGs) from redshift 1 to 2.5 and Riechers et al. (2014) presented one SMG at $z = 4.055$ have a consistent correlation between strong PAH features and the SFR. In recent JWST observation results, the galaxy at $z = 4.2248$ also presents strong PAH emission lines (Spilker et al. 2023). Shipley et al. (2016) gave a relation between the PAH peak luminosity and the star formation rate from Spitzer observations as

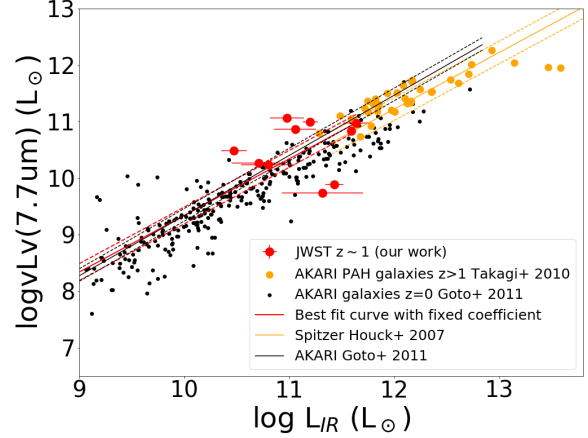


Figure 8. The $7.7 \mu m$ PAH peak luminosity versus total infrared luminosity. The red dots are our work based on JWST/MIRI. The orange dots are the AKARI results at $z > 1$ from (Takagi et al. 2010). The black dots are the results from Spitzer $8 \mu m$ at the local universe from (Goto et al. 2011). The black solid line was given in (Houck et al. 2007), which indicates the relation for starbursts and two black dashed lines were one sigma dispersion. The red solid line used the same coefficient in our data, the line located within 1 sigma deviation from the orange solid line. The red solid line is the least square fit for our work.

follows:

$$\log(SFR) = -42.84 + 0.995 \times \log(L_{PAH}), \quad (4)$$

and Kovács et al. (2019) gives a correlation from AKARI:

$$\log(SFR) = -41.55 + 0.98 \times \log(L_{PAH}). \quad (5)$$

L_{PAH} is the PAH peak luminosity $\nu L_{\nu}(7.7\mu m)$ in Eq. 2 from (Kovács et al. 2019), the red points are our work in which the SFRs are calculated by CIGALE SED fitting. In Fig. 9, we present the L_{PAH} and SFR calculated from CIGALE SED fitting for PAH luminous galaxies. In our work, the relation suggests a correlation between PAH luminosity and SFR, and the results are similar to Eq. 5 from (Shipley et al. 2016). However, there is no clear difference for the lower M and fainter L_{IR} galaxies at redshift ~ 1 compared to previous literature.

5 CONCLUSIONS

We utilise the JWST MIRI multi-wavelength photometry and the CANDELS EGS survey to select less luminous infrared galaxies that display prominent MIR PAHs beyond the reach of previous IR telescopes. We discover 10 PAH luminous galaxies out of a sample of 155 galaxies in the two CEERS fields with $\log(S_{15}/S_{10}) > 0.8$. We perform SED fitting on these galaxies using CIGALE models and 21 broad-band photometry from optical to mid-infrared. All of them have a good SED fitting result with a reduced chi-square (χ^2) < 6 . These galaxies are located at $z \sim 1$, and four of them are $L_{IR} < 10^{11} L_{\odot}$. All the properties of the selected PAH galaxies suggest that they are normal star-forming galaxies, rather than U/LIRGs. Our findings are summarised below.

- PAH galaxies we selected at redshift ~ 1 in Table 3 have infrared luminosity lower than $L_{IR} < 10^{12}$. JWST provides us with

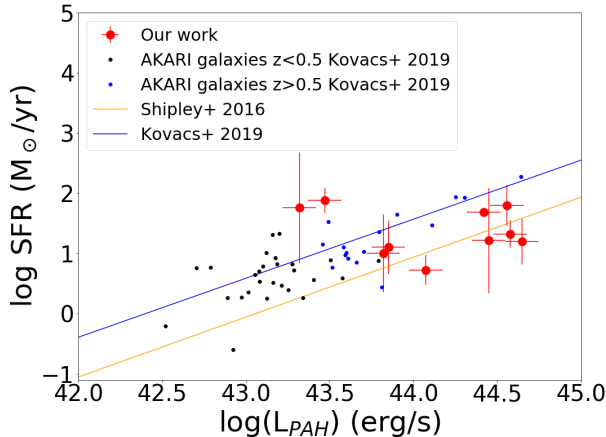


Figure 9. Correlation between PAH peak luminosity and SFR. Blue and black dots are *AKARI* sources from (Kovács et al. 2019). Blue solid line is the result from the *AKARI* telescope in Eq. 5 from (Kovács et al. 2019), and yellow solid line is the result from *Spitzer* in Eq. 4 from (Shipley et al. 2016).

the opportunity to investigate faint/normal PAH galaxies, rather than ULIRGs/LIRGs at $z \sim 1$.

- The selected PAH galaxies fall into the star-forming regions according to criteria from Kirkpatrick et al. (2017) in the $S_{15}/S_{7.7-8}/S_{18}/S_{10}$ colour space.

- The selected PAH galaxies lie on the SF main sequence at $z \sim 1$, with a stark contrast to ULIRGs, which often lie above the main sequence.

- The L_{PAH} versus L_{IR} in Fig. 8 shows a consistent relation with the known work for ULIRGs. This may indicate that the redshift and luminosity do not impact the PAH luminosity and strength. However, it is important to use a statistical sample to make the conclusion.

As we have shown a glimpse, the JWST has opened a new window to investigate faint/normal PAH galaxies at $z \sim 1$. With more JWST observations in the near future, the nature of PAH emissions in normal star-forming galaxies will be revealed further.

ACKNOWLEDGEMENTS

The authors express their gratitude to the anonymous referee for providing numerous constructive comments that have significantly enhanced the quality of this paper. TG acknowledges the support of the National Science and Technology Council of Taiwan through grants 108-2628-M-007-004-MY3, 111-2112-M-007-021, and 112-2112-M-007-013, and 112-2123-M-001-004. TH acknowledges the support of the National Science and Technology Council of Taiwan through grants 110-2112-M-005-013-MY3, 110-2112-M-007-034-, and 112-2123-M-001-004-. SH acknowledges the support of The Australian Research Council Centre of Excellence for Gravitational Wave Discovery (OzGrav) and the Australian Research Council Centre of Excellence for All Sky Astrophysics in 3 Dimensions (ASTRO 3D), through project number CE17010000 and CE170100013, respectively. This work used high-performance computing facilities operated by the Center for Informatics and Computation in Astronomy (CICA) at National Tsing Hua University. This equipment was funded by the Ministry of Education of Taiwan, the National Science and Technology Council of Taiwan, and National Tsing Hua University.

DATA AVAILABILITY

Early Release Observations obtained by JWST MIRI are publicly available at <https://www.stsci.edu/jwst/science-execution/approved-programs/webb-first-image-observations>.

REFERENCES

- Armus L., Charmandaris V., Soifer B. T., 2020, *Nature Astronomy*, 4, 467
- Ashby M. L. N., et al., 2015, *The Astrophysical Journal Supplement Series*, 218, 33
- Bielby, R. et al., 2012, *A&A*, 545, A23
- Boquien M., Burgarella D., Roehlly Y., Buat V., Ciesla L., Corre D., Inoue A. K., Salas H., 2019, *A&A*, 622, A103
- Brammer G. B., et al., 2012, *The Astrophysical Journal Supplement Series*, 200, 13
- Bruzual G., Charlot S., 2003, *MNRAS*, 344, 1000
- Buat V., Boquien M., Małek K., Corre D., Salas H., Roehlly Y., Shirley R., Efstathiou A., 2018, *A&A*, 619, A135
- Candian A., Zhen J., Tielens A. G. G. M., 2018, *Physics Today*, 71, 38
- Charlot S., Fall S. M., 2000, *ApJ*, 539, 718
- Chasteney J., et al., 2023a, *The Astrophysical Journal Letters*, 944, L11
- Chasteney J., et al., 2023b, *The Astrophysical Journal Letters*, 944, L12
- Desai V., et al., 2007, *ApJ*, 669, 810
- Draine B. T., et al., 2014, *ApJ*, 780, 172
- Elbaz D., Le Floc'h E., Dole H., Marcellac D., 2005, *A&A*, 434, L1
- Elbaz D., et al., 2007, *A&A*, 468, 33
- Elbaz D., et al., 2011, *A&A*, 533, A119
- Falstad N., et al., 2021, *A&A*, 649, A105
- Finkelstein S. L., et al., 2017, The Cosmic Evolution Early Release Science (CEERS) Survey, JWST Proposal ID 1345. Cycle 0 Early Release Science
- Fritz J., Franceschini A., Hatziminaoglou E., 2006, *MNRAS*, 366, 767
- García-Bernete I., Rigopoulou D., Alonso-Herrero A., Pereira-Santaella M., Roche P. F., Kerkeni B., 2022a, *MNRAS*, 509, 4256
- García-Bernete I., Rigopoulou D., Aalto S., Spoon H. W. W., Hernán-Caballero A., Efstathiou A., Roche P. F., König S., 2022b, *A&A*, 663, A46
- García-Bernete I., et al., 2022c, *A&A*, 666, L5
- Gardner J. P., et al., 2006, *Space Sci. Rev.*, 123, 485
- Gardner J. P., et al., 2023, *Publications of the Astronomical Society of the Pacific*, 135, 068001
- Gordon K. D., Clayton G. C., Declair M., Fitzpatrick E. L., Massa D., Misselt K. A., Tollerud E. J., 2023, *ApJ*, 950, 86
- Goto T., et al., 2011, *MNRAS*, 410, 573
- Gwyn S. D. J., 2012, *AJ*, 143, 38
- Houck J. R., Weedman D. W., Floc'h E. L., Hao L., 2007, *The Astrophysical Journal*, 671, 323
- Hsiao T. Y.-Y., et al., 2023a, *arXiv e-prints*, p. arXiv:2305.03042
- Hsiao T. Y.-Y., et al., 2023b, *ApJ*, 949, L34
- Huang J. S., et al., 2023, *ApJ*, 949, 83
- Hummer D. G., Storey P. J., 1987, *Monthly Notices of the Royal Astronomical Society*, 224, 801
- Kalirai J., 2018, *Contemporary Physics*, 59, 251
- Kennicutt Robert C. J., 1998, *ARA&A*, 36, 189
- Kim S. J., et al., 2019, *PASJ*, 71, 11
- Kirkpatrick A., Pope A., Sajina A., Roebuck E., Yan L., Armus L., Díaz-Santos T., Stierwalt S., 2015, *The Astrophysical Journal*, 814, 9
- Kirkpatrick A., et al., 2017, *The Astrophysical Journal*, 849, 111
- Koekemoer A. M., et al., 2011, *The Astrophysical Journal Supplement Series*, 197, 36
- Kovács T. O., Burgarella D., Kaneda H., Molnár D. C., Oyabu S., Pinter S., Toth L. V., 2019, *PASJ*, 71, 27
- Kwok S., 2022, *Ap&SS*, 367, 16
- Li A., 2020, *Nature Astronomy*, 4, 339
- Ling C.-T., et al., 2022, *Monthly Notices of the Royal Astronomical Society*, 517, 853

Lo Faro B., Buat V., Roehly Y., Alvarez-Marquez J., Burgarella D., Silva L., Efstathiou A., 2017, *Monthly Notices of the Royal Astronomical Society*, 472, 1372

Malek, K. et al., 2018, *A&A*, 620, A50

McElwain M. W., et al., 2023, *Publications of the Astronomical Society of the Pacific*, 135, 058001

Pearson, W. J. et al., 2018, *A&A*, 615, A146

Peeters E., Tielens A. G. G. M., Allamandola L. J., Bauschlicher C. W., Boogert A. C. A., Hayward T. L., Hudgins D. M., Sandford S. A., 2003, in Witt A. N., ed., *Astrophysics of Dust*. p. 42

Peeters E., Mattiouda A. L., Kemper F., Hudgins D. M., Allamandola L. J., 2006, in Armus L., Reach W. T., eds, *Astronomical Society of the Pacific Conference Series Vol. 357, The Spitzer Space Telescope: New Views of the Cosmos*. p. 95 ([arXiv:astro-ph/0507008](https://arxiv.org/abs/astro-ph/0507008)), doi:10.48550/arXiv.astro-ph/0507008

Polletta M., et al., 2007, *ApJ*, 663, 81

Pope A., et al., 2008, *ApJ*, 675, 1171

Popesso P., et al., 2023, *MNRAS*, 519, 1526

Rich J., et al., 2023, *ApJ*, 944, L50

Riechers D. A., et al., 2014, *ApJ*, 786, 31

Rieke G. H., et al., 2015, *Publications of the Astronomical Society of the Pacific*, 127, 584

Rigopoulou D., Spoon H. W. W., Genzel R., Lutz D., Moorwood A. F. M., Tran Q. D., 1999, *AJ*, 118, 2625

Salpeter E. E., 1955, *ApJ*, 121, 161

Santos D. J. D., et al., 2021, *MNRAS*, 507, 3070

Shipley H. V., Papovich C., Rieke G. H., Brown M. J. I., Moustakas J., 2016, *The Astrophysical Journal*, 818, 60

Skelton R. E., et al., 2014, *The Astrophysical Journal Supplement Series*, 214, 24

Spilker J. S., et al., 2023, *Nature*, 618, 708

Stefanon M., et al., 2017, *The Astrophysical Journal Supplement Series*, 229, 32

Takagi T., et al., 2010, *A&A*, 514, A5

Takagi T., Matsuhara H., Wada T., Ohya Y., 2011, *Proceedings of the International Astronomical Union*, 7, 456–459

Tielens A. G. G. M., 2008, *ARA&A*, 46, 289

Wang T.-W., et al., 2020, *MNRAS*, 499, 4068

Weedman D. W., Houck J. R., 2008, *The Astrophysical Journal*, 686, 127

Whitaker K. E., van Dokkum P. G., Brammer G., Franx M., 2012, *The Astrophysical Journal Letters*, 754, L29

Wright G. S., et al., 2023, *Publications of the Astronomical Society of the Pacific*, 135, 048003

Wu C. K. W., et al., 2023, *MNRAS*, 523, 5187

APPENDIX A: SED RESULT

In Sec.3, we present the SED fitting result in Fig. 3. We present other SED fit results in A1-A11. In Table A1, we present six photometric data from JWST MIRI observation.

This paper has been typeset from a \LaTeX file prepared by the author.

Table A1. Flux densities and errors for PAH selected galaxies observed by JWST. Note that the unit of flux densities is μJy . There are 10 good fitting sources ($\chi < 6$) and 2 bad fitting sources. The other 15 broad-band photometric data are from CANDELS-EGS catalog (Finkelstein et al. 2017), described in Sec.2.1.

ID	Name in CANDELS_EGS	F770W		F1000W		F1280W		F1500W		F1800W		F2100W	
		f_ν	Δf_ν										
59	CANDELS_EGS_F160W_J142040.3+530306.6	3.45	0.30	3.10	0.33	23.65	2.88	37.55	3.92	31.14	4.39	14.41	1.94
64	CANDELS_EGS_F160W_J142037.9+530249.5	1.20	0.11	0.74	0.09	3.46	0.43	7.20	0.76	5.97	0.91	10.12	1.49
66	CANDELS_EGS_F160W_J142038.3+530254.9	11.93	1.03	10.00	1.05	50.01	6.08	118.25	12.33	99.52	14.00	15.86	2.10
72	CANDELS_EGS_F160W_J142038.5+530306.1	2.93	0.25	2.36	0.25	13.92	1.69	28.60	2.98	29.40	4.15	7.39	1.23
113	CANDELS_EGS_F160W_J142039.1+530351.7	4.70	0.41	4.82	0.51	13.58	1.65	36.80	3.84	211.84	29.79	57.72	7.08
136	CANDELS_EGS_F160W_J142034.8+530329.6	7.93	0.69	10.09	1.06	28.72	3.49	78.93	8.23	146.53	20.61	33.05	4.11
178	CANDELS_EGS_F160W_J142022.8+525859.5	8.14	0.70	6.70	0.70	20.89	2.54	44.31	4.62	94.34	13.27	28.74	3.60
187	CANDELS_EGS_F160W_J142018.2+525825.4	7.38	0.64	6.38	0.67	18.66	2.27	48.55	5.06	108.60	15.27	30.71	3.84
218	CANDELS_EGS_F160W_J142020.3+525925.1	2.49	0.22	1.67	0.18	10.17	1.24	19.46	2.03	16.74	2.38	3.56	0.96
225	CANDELS_EGS_F160W_J142016.5+525859.9	1.02	0.09	0.87	0.10	4.50	0.56	10.22	1.08	7.00	1.04	14.32	1.93
145	CANDELS_EGS_F160W_J142033.6+530323.4	1.23	0.11	1.20	0.13	7.49	0.91	9.57	1.01	3.88	0.64	3.68	0.95
250	CANDELS_EGS_F160W_J142017.0+525938.8	0.69	0.06	3.98	0.42	3.99	0.49	3.24	0.37	3.64	0.61	5.97	1.10

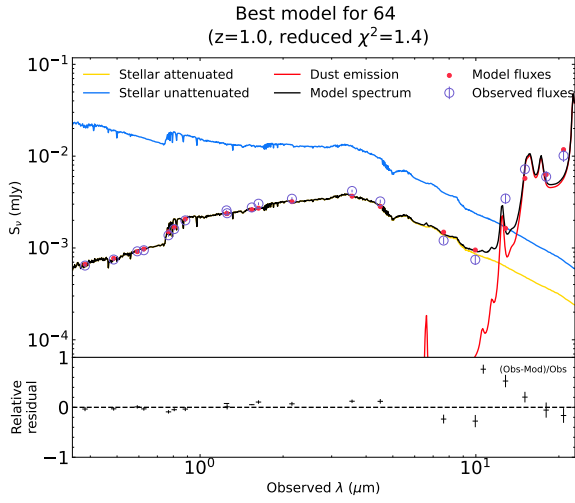


Figure A1. The same as Fig. 3, but for ID 64

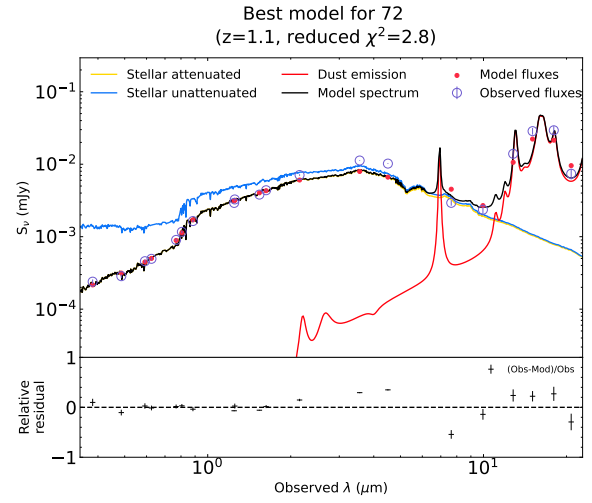


Figure A3. The same as Fig. 3, but for ID 72

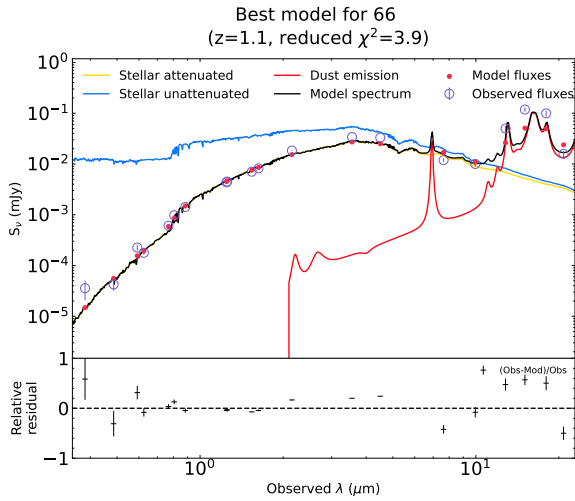


Figure A2. The same as Fig. 3, but for ID 66

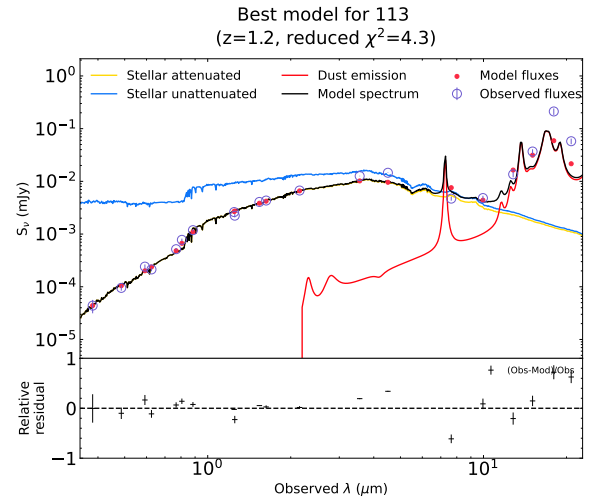


Figure A4. The same as Fig. 3, but for ID 113.

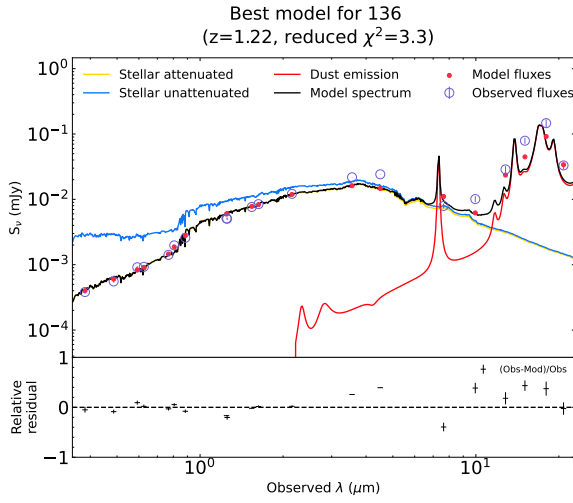


Figure A5. The same as Fig. 3, but for ID 136.

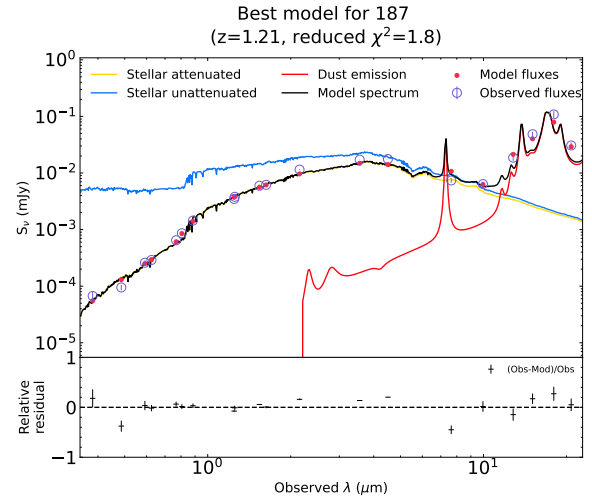


Figure A7. The same as Fig. 3, but for ID 187.

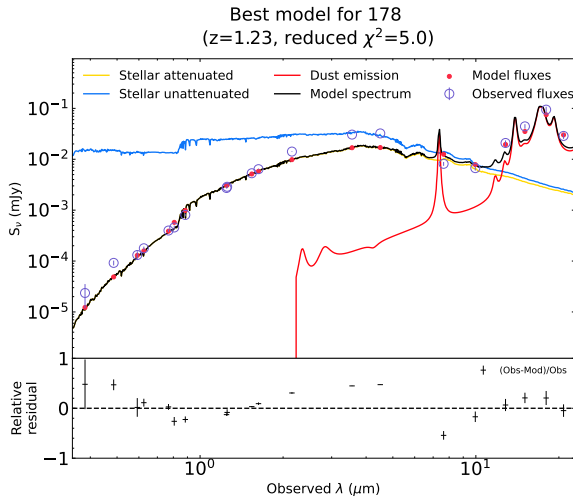


Figure A6. The same as Fig. 3, but for ID 178.

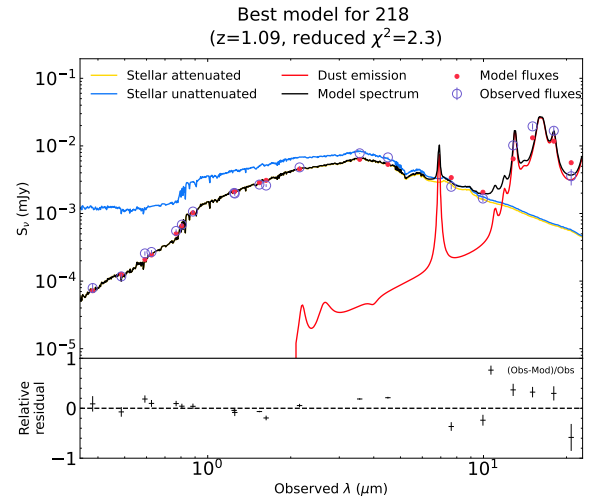


Figure A8. The same as Fig. 3, but for ID 218.

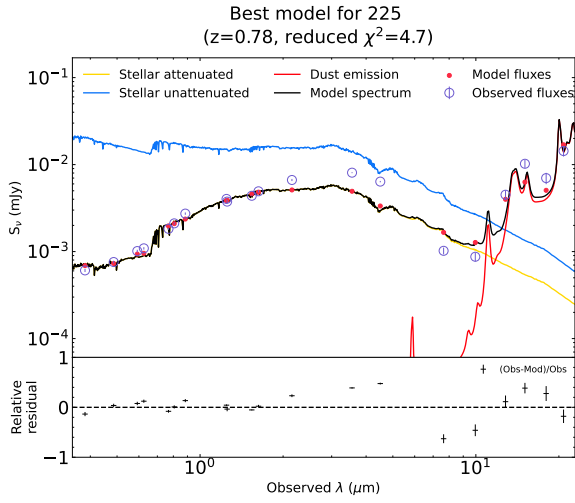


Figure A9. The same as Fig. 3, but for ID 225.

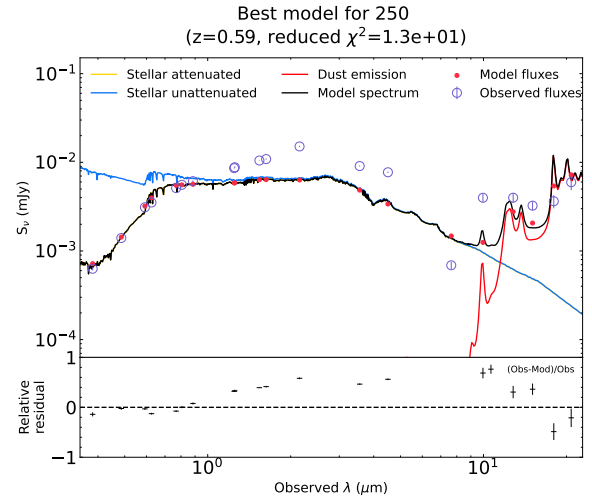


Figure A11. The same as Fig. 3, but for ID 250.

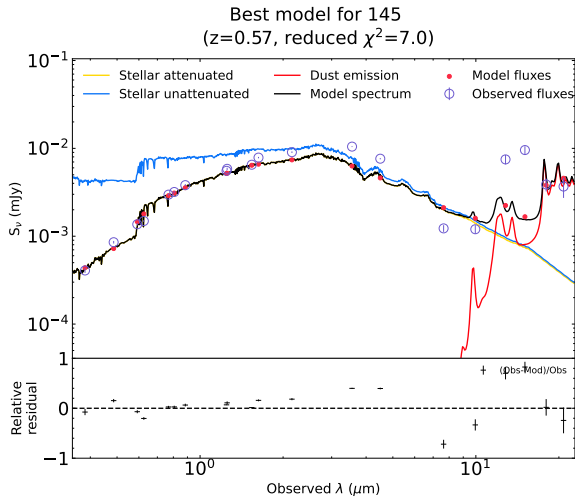


Figure A10. The same as Fig. 3, but for ID 145.